33rd Annual International Conference of the IEEE EMBS
Boston, Massachusetts USA, August 30 - September 3, 2011

3D Segmentation of Keratin Intermediate Filaments in Confocal Laser Scanning Microscopy

Gerlind Herberich*, Reinhard Windoffer**, Rudolf Leube** and Til Aach*

Abstract— **In this paper, we propose and compare different methods for the 3D segmentation of keratin intermediate filaments (KFs) in images acquired using confocal laser scanning microscopy (CLSM). KFs are elastic cables forming a complex scaffolding within epithelial cells. They are involved in many basic cell functions. To understand the mechanisms of filament formation and network organisation under physiological and pathological conditions, quantitative measurements of dynamic network alterations are essential. Segmenting KFs is a key component for analyzing their dynamic and biomechanical properties. KFs were labeled with fluorescent keratins to allow high resolution imaging of network dynamics in native cells. Our segmentation methods follow the principle of ridge enhancement filtering and subsequent centerline extraction. The evaluation of the methods is two-fold: (i) We develop synthetic data that exhibit the characteristics of real CLSM data to evaluate the precision of the different methods in terms of centerline localisation and (ii) we perform a connected component analysis on the segmentation results of real KF data to assess whether the connectivity of highly complex networks is being preserved by the segmentation. Our evaluation shows that in the presence of strong noise and despite the highly anisotropic spatial resolution of CLSM images the proposed method is able to accurately localize the centerlines of the KFs and to preserve the KF networks' connectivity. Taken together this is a strong indicator that also the network topology is being preserved.**

I. INTRODUCTION

4D (3D+time) live cell fluorescence imaging by confocal laser scanning microscopy (CLSM) has become a widely used tool in cell biology for the analysis of the dynamics of subcellular structures. In the work presented here, we investigate the properties of keratin intermediate filaments (KFs). They are flexible, filamentous structures of about 10 nm diameter forming a complex scaffolding within epithelial cells (Fig. 1). As part of the cytoskeleton, they are responsible for the mechanical stability of epithelial cells and tissues and are also involved in the regulation of many basic cell functions [1], [2].

The network topology is a key component for the analysis of dynamic KF behavior under different conditions. To this end, we have acquired 3D images of fluorescently-labeled KF networks by means of CLSM. In CLSM, the three-dimensional specimen is scanned slice by slice, each slice being scanned point-wise. The resulting image is a 3D stack of 2D slices. Due to the PSF of a CLSM, the spatial resolution of such a 3D image is highly limited in the dimension along the optical axis leading to a highly anisotropic spatial image resolution. Furthermore, the images are strongly corrupted by Photon-counting noise which is signal-dependent.

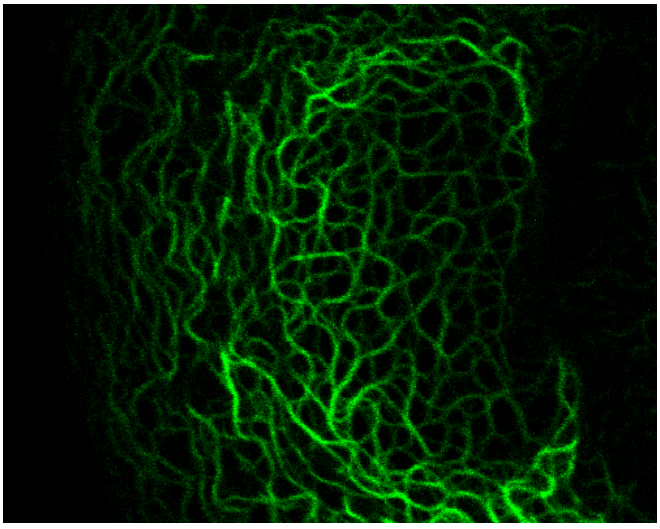

Fig. 1. 2D slice of the 3D scaffolding of fluorescently-labeled keratin intermediate filaments in a segment of a cultured epithelial cell acquired by confocal laser scanning microscopy. The keratin filaments appear as green elongated bended curves in the image.

To date methods are lacking for the 3D segmentation of subcellular filamentous structures whose diameter is close to or below the resolution limit in CLSM images. In the past, considerable effort has been invested in the 3D segmentation of structures at the supracellular level, which can be imaged with a high spatial resolution in all three dimensions. Concerning bended elongated structures, numerous vessel segmentation approaches have been proposed. However, it has not yet been assessed whether these algorithms are able to cope with data that exhibit a critically low spatial resolution in the third dimension. Another challenge for the segmentation of KFs compared to vessel segmentation is the huge variability of KF network branchings. Preserving these branchings in the segmentation result is crucial to preserving the network topology. To the best of our knowledge, approaches to the segmentation of subcellular filamentous structures have only been developed in 2D, thus ignoring the fact that the structures' dynamics are inherently 3-dimensional: e.g. in [3] a method for the 2D segmentation of wide-field fluorescence image data of microtubules and actin filaments relying on rotated matched filtering has been proposed. In [4], microtubules in wide-field fluorescence microscopic images are segmented using a more precise

*Institute of Imaging & Computer Vision, RWTH Aachen University, 52056 Aachen, Germany
**Institute of Molecular & Cellular Anatomy, RWTH Aachen University, 52056 Aachen, Germany

and efficient steerable ridge enhancement and centerline extraction approach.

Our contribution is organized as follows: Towards the 3D segmentation of KF networks in CLSM images, we propose to follow the principle of line enhancement filtering and centerline extraction. Three line enhancement filtering approaches [5], [6], [7] together with one centerline extraction algorithm [8] yield three different segmentation approaches. The methods are briefly summarized in Section II. In Section III, we conduct a thorough comparison of the three different segmentation methods using synthetic data that reflect the characteristic properties of CLSM image data: intensity-dependent noise and highly anisotropic spatial resolution. Furthermore, we validate the proposed method on real CLSM images by means of a connected component analysis to assess whether the KF network connectivity is preserved.

II. METHODS

A. Ridge enhancement filtering

For ridge enhancement we compare [5], [6] and [7].

1) Steerable curve detection [5]: The steerable 3D curve detector [5], [9] is built from derivatives of Gaussians and therefore separable. It is designed to optimize on the one hand signal-to-noise ratio and on the other hand ridge localization by maximizing the second derivative of the filter response orthogonal to the feature boundary. The detector satisfiying these optimality criteria for a bright line on dark background oriented along the x-axis is

$$h_{curve} = \frac{1}{2\sqrt{2\pi}}\left(\frac{2}{3}g_{xx} - g_{yy} - g_{zz}\right) \tag{1}$$

with g_{xx}, g_{yy} and g_{zz} being the partial second derivatives of a 3D Gaussian in x, y and z respectively. Reformulating this detector as a steerable filter to detect arbitrarily oriented ridges (see [5] sec. 2.3), we can determine the ridge strength - i.e. the filter response - at a given image position as a function of orientation. Maximizing this expression with respect to the orientation angle simultaneously yields an estimation of the optimal ridge orientation which can be determined analytically.

2) Ridge enhancement filter by Frangi et al. [6]: This filter relies on an eigensystem analysis of the Hessian matrix of the image which we briefly summarize in the following. Let the eigenvalues of the Hessian matrix be ordered according to $|\lambda_1| \leq |\lambda_2| \leq |\lambda_3|$. Then, at locations of tubular structures the following conditions will hold: $|\lambda_1| \approx 0$, $|\lambda_1| \ll |\lambda_2|$ and $\lambda_2 \approx \lambda_3$. In particular, for bright tubular structures surrounded by dark background as is the case for fluorescently-labeled filaments, $\lambda_2 < 0$ and $\lambda_3 < 0$. The vesselness measure proposed by Frangi et al. is defined as follows

$$\mathscr{V}_{\mathscr{F}} = \begin{cases} (1-\exp(-\frac{\mathscr{R}_{\mathscr{A}}{}^2}{2\alpha^2}))\exp(-\frac{\mathscr{R}_{\mathscr{B}}{}^2}{2\beta^2})(1-\exp(-\frac{\mathscr{S}^2}{2c^2})) \\ 0 \qquad\qquad \text{if } \lambda_2 > 0 \text{ or } \lambda_3 > 0 \end{cases} \tag{2}$$

with α, β and c being parameters that control the sensitivity of the filter to the measures $\mathscr{R}_{\mathscr{A}} = \frac{|\lambda_2|}{|\lambda_3|}$, $\mathscr{R}_{\mathscr{B}} = \frac{|\lambda_1|}{\sqrt{|\lambda_2\lambda_3|}}$ and $\mathscr{S} = \sqrt{\sum_j \lambda_j^2}$. $\mathscr{R}_{\mathscr{B}}$ becomes maximal for blob-like structures and zero for $|\lambda_1| \approx 0$. As it cannot differentiate between line-like and plate-like structures, $\mathscr{R}_{\mathscr{A}}$ is introduced. Finally, $\mathscr{S}$ shall avoid filter responses from noise by accounting for the norm of the Hessian matrix, i.e., for the magnitude of the derivatives which is low for noise and large for structures.

3) Ridge enhancement filter by Sato et al. [7]: This filter also relies on an eigensystem analysis of the Hessian:

$$\mathscr{V}_{\mathscr{S}} = \begin{cases} |\lambda_3|(\frac{\lambda_2}{\lambda_3})^{\gamma_{23}}(1+\frac{\lambda_1}{|\lambda_2|})^{\gamma_{12}} & , \lambda_3 < \lambda_2 < \lambda_1 \leq 0 \\ |\lambda_3|(\frac{\lambda_2}{\lambda_3})^{\gamma_{23}}(1-\alpha\frac{\lambda_1}{|\lambda_2|})^{\gamma_{12}} & , \lambda_3 < \lambda_2 < 0 < \lambda_1 < \frac{|\lambda_2|}{\alpha} \\ 0 & \text{otherwise} \end{cases} \tag{3}$$

Here, $\gamma_{23} \geq 0$ controls cross-section isotropy in order to distinguish between line-like and plate-like structures. Deviation from the condition $|\lambda_1| \approx 0$ is penalized by means of $\gamma_{12} \geq 0$ and $0 < \alpha \leq 1$ such that blob-like structures are suppressed.

B. Centerline extraction

To obtain a binary segmentation, our goal is to extract a one-pixel wide centerline from the enhanced ridges while preserving the connectivity of the network. To this end, we threshold the ridge strength image to obtain a binary volume segmentation and use the thinning algorithm proposed in [8], [10] for centerline extraction.

The threshold is an adaptive threshold computed from the Otsu threshold [11]. Note that the only requirement for this thresholding step is the preservation of connectivity. The Otsu threshold itself, however, does not achieve this for the response of all three filters. Therefore, we automatically compute a suitable threshold that satisfies this requirement by increasing or decreasing the Otsu threshold by a certain percentage that is fixed for each filter.

The subsequent centerline extraction algorithm iteratively thins the binary volume segmentation by performing several tests for each voxel to test if it can be deleted from the object without leading to a shortening of the centerline or a destruction of connectivity [8], [10].

III. EVALUATION

A. Evaluation based on synthetic data

To assess the precision of the different methods with respect to centerline localisation, we have developed synthetic image data. The basis for the synthetic image data is a 3D network of 7 tubular structures of radius 3 with different kinds of branchings (Fig. 2). The network exhibits a total length of 667 centerline points. From this 3D network, different image data are generated.

1) Generation of synthetic images: The generation of the synthetic image data consists of the simulation of the following three aspects:

- CLSM PSF modeled by an anisotropic 3D Gaussian
- anisotropic spatial sampling of the 3D object
- photon-counting noise modeled by a Poisson distribution

The anisotropic spatial sampling - i.e. the resulting voxel size - chosen for the image acquisition is directly related to the

Fig. 2. Maximum-Intensity-Projection of the synthetic 3D network.

CLSM PSF as the PSF limits the resolution. The CLSM PSF can be modeled by a 3D-Gaussian [12]. The image data we have acquired with our Zeiss confocal microscope (LSM710) exhibit in the worst case voxels of $VoxelSizeXY = 66nm$ in the dimensions of the image plane and $VoxelSizeZ = 396nm$ in the dimension along the optical axis which is a sampling anisotropy of $SA = \frac{VoxelSizeZ}{VoxelSizeXY} = 6$ between the third dimension and the other two dimensions. To assess the influence of the anisotropic spatial resolution on the precision of the segmentation result, we generate 6 data sets with sampling anisotropy from $SA = 1$ (isotropic spatial sampling) to $SA = 6$. Simultaneously, we change the support of the Gaussian PSF model in the third dimension from isotropic (equal standard deviation in all dimensions $\sigma_x = \sigma_y = \sigma_z$) to anisotropic ($\sigma_z = 6 \cdot \sigma_x$) while the standard deviations in the dimensions of the image plane remain constant. Finally, Poisson noise is added to the data.

2) Error measures: For the above data sets, we evaluate voxel-wise centerline overlap (Fig. 3) and mean Euclidean distance between reference centerline and segmentation result (Fig. 4). Note that the mean Euclidean distance is dimensionless here because the voxel size of our synthetic data sets is dimensionless. The fact that the mean Euclidean distance is small also for highly anisotropic voxels clearly shows that the deviation of the segmented centerline from the true centerline position is very small and that allowing a small tolerance region around the reference centerline in the overlap measure would lead to a significantly increased overlap compared to the hard voxel-wise overlap measure in Fig. 3. In addition, we verified that for all data sets, the connectivity is preserved. Furthermore, we visually assessed the segmentation results with respect to artefacts such as knobs or loops. The segmentations relying on the Frangi filter and the segmentations relying on the steerable curve detector are mostly free of artefacts. The segmentations relying on the Sato filter tend to contain little knobs, where the segmentation result is not a one-pixel-wide line.

B. Evaluation on real data

To assess the performance of the segmentation methods on real KF networks that exhibit a higher complexity than the synthetic data, we (i) perform a connected component analysis on the segmentation results and (ii) assess the results visually. Sorting the connected components in order of decreasing size shows that the network connectivity has been preserved for all three methods. As an example, Fig. 5 shows in the upper left image the KF network of an entire cell in the middle and a part of KF networks of two other cells, one in the upper left corner and the other one at the top of the image. The segmentation result using the Frangi filter is shown in the upper right image. In the lower row, the two largest connected components are shown. As expected, the largest component is the segmentation of the KF network of the cell in the center and the second largest component is the segmentation of the KF network of the cell in the upper left corner. A visual assessment of the segmentation results of the three methods shows that also for KF images, the Sato method tends to form knobs and other artefacts. The steerable curve detector method produces significantly less artefacts while the results from the Frangi method clearly outperform the latter.

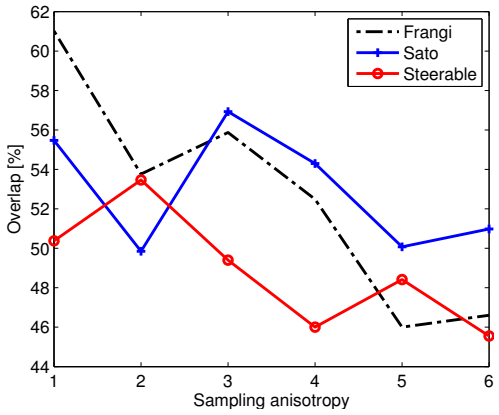

Fig. 3. Voxel-wise overlap of reference centerline and segmentation result for the three segmentation methods indicated in percent.

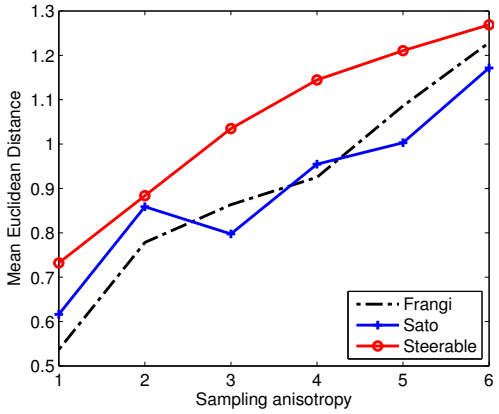

Fig. 4. Mean Euclidean distance of reference centerline and segmentation result for the three segmentation methods. Note that the mean Euclidean distance is dimensionless as the voxel size of the synthetic data is dimensionless.

IV. CONCLUSIONS

In this contribution, we have proposed line enhancement filtering, adaptive thresholding and centerline extraction for the 3D segmentation of KFs in CLSM images. We have compared the performance of three different line enhancement

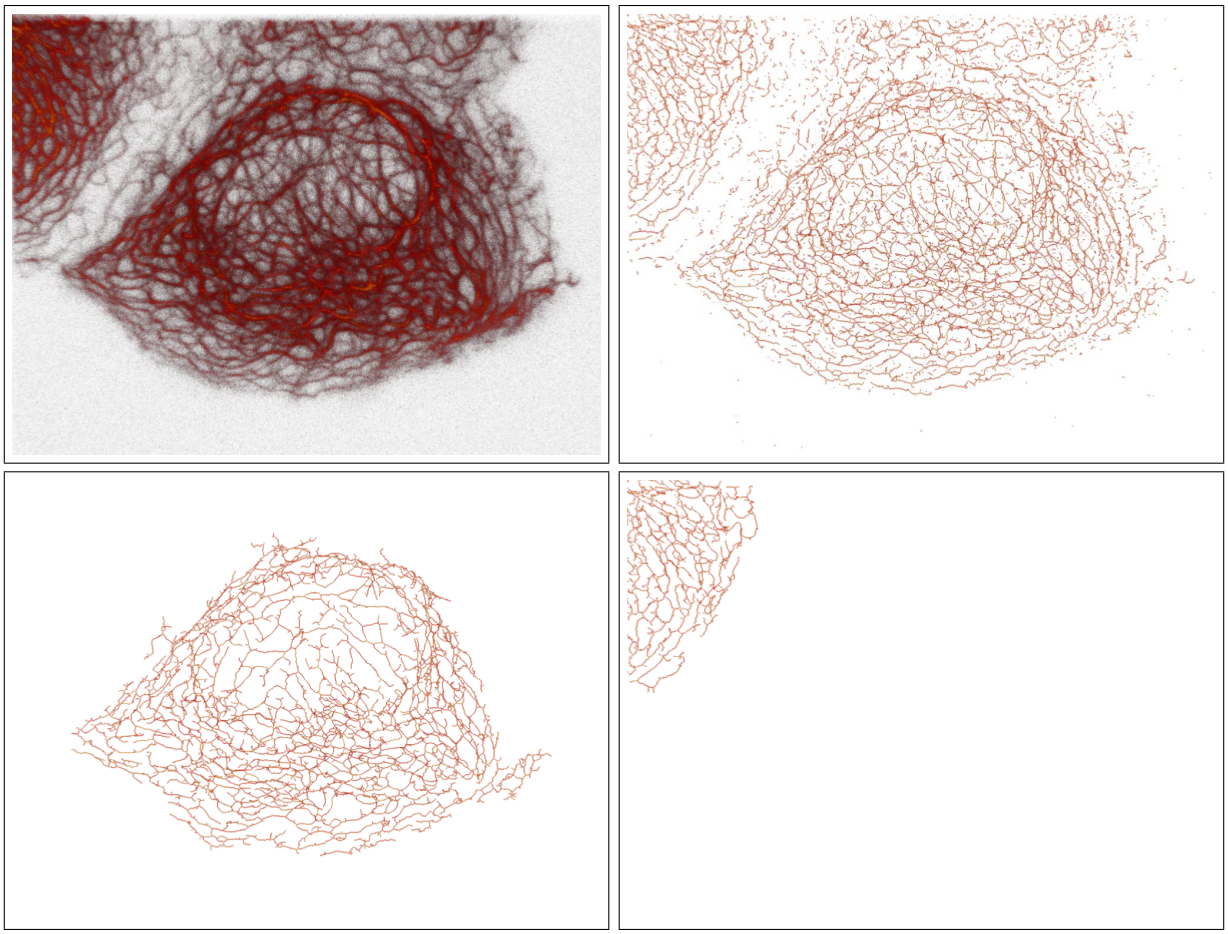

Fig. 5. Upper row: Maximum-Intensity-Projection (MIP) of a 3D image showing the KF network of a cell in the center and a part of KF networks of two other cells in the upper left corner and at the top of the image (left). MIP of the segmentation result using the Frangi filter (right). Lower row: MIP of the largest connected component of the segmentation result (left) and MIP of the second largest connected component of the segmentation result (right).

filters in combination with a centerline extraction method using synthetic data that reflects the critical properties of real CLSM data. The results show that all three methods are able to accurately localize the sought centerlines despite highly anisotropic image resolution and in the presence of strong noise. In images of real KF networks, the network connectivity is preserved by all three methods. A visual assessment reveals that the segmentation results relying on the Frangi filter produce the best centerlines while the results relying on the Sato filter or the steerable curve detector exhibit a few knobs or loops.

V. ACKNOWLEDGMENTS

The authors gratefully acknowledge for funding by the German Research Council (DFG, AA5/5-1, LE566/18-1, WI1731/8-1).

REFERENCES

[1] R. E. Leube, M. Moch, and R. Windoffer, "Panta rhei: Perpetual cycling of the keratin cytoskeleton," *BioArchitecture*, vol. 1(1), pp. 39–44, 2011.

[2] T. Magin, P. Vijayaraj, and R. Leube, "Structural and regulatory functions of keratins." *Exp Cell Res*, vol. 313(10), pp. 2021–32, 2007.

[3] N. Lichtenstein, B. Geiger, and Z. Kam, "Quantitative analysis of cytoskeletal organization by digital fluorescent microscopy." *Cytometry A*, vol. 54, no. 1, pp. 8–18, Jul 2003.

[4] G. Herberich, A. Ivanescu, I. Gamper, A. Sechi, and T. Aach, "Analysis of length and orientation of microtubules in wide-field fluorescence microscopy," in *Pattern Recognition, Proceedings of the 32nd DAGM*, M. Goesele and S. Roth, Eds. Springer LNCS, September 22–24 2010, pp. 182–191.

[5] F. Aguet, M. Jacob, and M. Unser, "Three-dimensional feature detection using optimal steerable filters," in *Proc. IEEE Int. Conf. Image Processing ICIP 2005*, vol. 2, 2005.

[6] A. Frangi, W. Niessen, K. Vincken, and M. Viergever, "Multiscale vessel enhancement filtering," in *Medical Image Computing and Computer-Assisted Intervention*, 1998, pp. 130–137.

[7] Y. Sato, S. Nakajima, N. Shiraga, H. Atsumi, S. Yoshida, T. Koller, G. Gerig, and R. Kikinis, "Three-dimensional multi-scale line filter for segmentation and visualization of curvilinear structures in medical images," *Medical Image Analysis*, vol. 2, no. 2, pp. 143 – 168, 1998.

[8] T. C. Lee, R. L. Kashyap, and C. N. Chu, "Building skeleton models via 3-d medial surface axis thinning algorithms," *CVGIP: Graphical Models and Image Processing*, vol. 56, no. 6, pp. 462 – 478, 1994.

[9] M. Jacob and M. Unser, "Design of steerable filters for feature detection using canny-like criteria," *IEEE Transactions on Pattern Analysis and Machine Intelligence*, vol. 26, pp. 1007–1019, 2004.

[10] H. Homann, "Implementation of a 3d thinning algorithm," *MIDAS Insight Journal*, 2007. [Online]. Available: http://hdl.handle.net/1926/1292

[11] N. Otsu, "A threshold selection method from gray-level histograms," *IEEE Transactions on systems, man, and cybernetics*, vol. SMC-9, pp. 62–66, 1979.

[12] B. Zhang, J. Zerubia, and J.-C. Olivo-Marin, "Gaussian approximations of fluorescence microscope point-spread function models," *Applied Optics*, vol. 46(10), pp. 1819–1829, 2007.